JGR Atmospheres

RESEARCH ARTICLE
10.1029/2020JD033969

Key Points:

- Tropical temperature variability is quantified using dense COSMIC-2 radio occultation measurements
- COSMIC-2 data reveal a rich spectrum of equatorial planetary waves and diurnal tides in the tropical lower stratosphere
- Small-scale temperature variances reveal coherent geophysical structures tied to convection and stratospheric Kelvin waves

Correspondence to:
W. J. Randel,
randel@ucar.edu

Citation:
Randel, W. J., Wu, F., & Podglajen, A. (2021). Equatorial waves, diurnal tides and small-scale thermal variability in the tropical lower stratosphere from COSMIC-2 radio occultation. *Journal of Geophysical Research: Atmospheres*, *126*, e2020JD033969. https://doi.org/10.1029/2020JD033969

Received 25 SEP 2020
Accepted 4 MAR 2021

Author Contributions:
Conceptualization: William J. Randel
Formal analysis: Fei Wu
Investigation: Aurélien Podglajen
Methodology: William J. Randel, Fei Wu
Software: Fei Wu
Supervision: William J. Randel
Writing – original draft: William J. Randel
Writing – review & editing: William J. Randel, Aurélien Podglajen

Equatorial Waves, Diurnal Tides and Small-Scale Thermal Variability in the Tropical Lower Stratosphere From COSMIC-2 Radio Occultation

William J. Randel[1,2], Fei Wu[1], and Aurélien Podglajen[3]

[1]National Center for Atmospheric Research, Boulder, CO, USA, [2]COSMIC Program, University Corporation for Atmospheric Research, Boulder, CO, USA, [3]Laboratoire de Météorologie Dynamique, Paris, France

Abstract A new constellation of radio occultation satellites called COSMIC-2 (Constellation Observing System for Meteorology, Ionosphere, and Climate-2) is providing unprecedented dense measurements of the tropical atmosphere, with on average more than 4,000 high quality observations per day over 40°N–S. We use these data to evaluate large- and small-scale thermal variability in the tropical lower stratosphere during October 2019 – April 2020. Space-time spectral analysis of 6-hourly gridded COSMIC-2 data reveals a rich spectrum of traveling planetary-scale waves, including Kelvin waves, mixed Rossby-gravity waves and inertia gravity waves, in addition to propagating diurnal tides. These coherent modes show enhanced amplitudes from the tropical tropopause through the lower stratosphere (~17–25 km). Characteristics of small-scale temperature variances, calculated as deviations from the gridded fields, reveal systematic spatial patterns including time average maxima over Africa and South America overlying frequent deep convection. Small-scale variances also exhibit transient maxima in the equatorial lower stratosphere tied to local variations in static stability, associated with large-scale Kelvin waves. The new COSMIC-2 observations provide novel details on the rich spectrum of large- and small-scale waves near and above the tropical tropopause.

Plain Language Summary A new constellation of radio occultation satellites called COSMIC-2 (Constellation Observing System for Meteorology, Ionosphere and Climate-2) is providing unprecedented dense measurements of the tropical atmosphere, with on average more than 4,000 high quality observations per day over 40°N–S. We use these data to provide novel understanding of temperature variability near the tropical tropopause and lower stratosphere (~10–30 km). COSMIC-2 data reveal a rich spectrum of large- and small-scale waves, including eastward- and westward-propagating planetary-scale equatorial waves and diurnal tides. The measurements also identify localized regions of enhanced temperature variability tied to small-scale gravity waves. These new measurements are valuable for constraining global models and understanding water vapor and high-level clouds in the tropics.

1. Introduction

Large-scale equatorial waves contribute a dominant fraction of variance for meteorological fields in the tropical upper troposphere and lower stratosphere (UTLS). These waves are important for their organized contributions to UTLS circulation, constituent transport, stratospheric dehydration and cloud formation processes. For example, Chang & L'Ecuyer, 2020; Fujiwara et al., 2001, 2009; Jensen & Pfister, 2004; Kim et al., 2016; Mote & Dunkerton, 2004; Podglajen et al., 2018; Ueyama et al., 2015. Additionally, UTLS equatorial waves propagate vertically and provide important forcing for the stratospheric quasi-biennial oscillation (QBO) and semi-annual oscillation (SAO), and hence it is important to quantify wave behavior in observations and use measurements to evaluate and constrain models (e.g., Kawatani et al., 2009; Holt et al., 2016, 2020).

Satellites provide key observations for characterizing equatorial waves. An important aspect of equatorial waves is their relatively narrow vertical scales (typical vertical wavelengths of ~4–8 km), so that high vertical resolution is important for satellite measurements. Temperature retrievals from Global Navigation Satellite System (GNSS) radio occultation (RO) have UTLS vertical resolution of ~1 km or better (Zeng et al., 2019), with horizontal (along-track) resolution of ~200 km, and global measurements since ~2002 have provided characterization of equatorial wave structure and long-term variability (e.g., Alexander et al., 2008; Kim

& Son, 2012; Randel & Wu, 2005; Scherllin-Pirscher et al., 2017, 2021; Tsai et al., 2004). Complementary studies with other high resolution satellite data were provided by Alexander and Ortland (2010) and Ern et al. (2008), and numerous studies have analyzed UTLS equatorial waves in meteorological reanalyzes (e.g., Kim et al., 2019, and references therein).

The focus of this work is an analysis of thermal variability in the tropical lower stratosphere using the dense, high quality RO measurements from the COSMIC-2 constellation, launched in June 2019. COSMIC-2 (hereafter C2) is a set of 6 satellites in low inclination Earth orbit, which will provide ~5,000 occultations per day over low latitudes (40°N–S) when fully operational. C2 satellites have improved receivers that provide enhanced signal-to-noise ratio compared to previous RO missions (Schreiner et al., 2020), and we use the high quality data to provide a novel look at UTLS thermal variability during the first several months of observations (October 2019–April 2020). In addition to analyses of large-scale gridded fields, the concentrated sampling of C2 provides opportunity to evaluate smaller-scale variability (i.e., deviations from the analyzed large-scale structure), and we highlight interesting coherent behavior of the small scale temperature variances in these new data.

2. Data and Analyses

The six-satellite C2 constellation has been providing on average more than 4,000 RO profiles per day since September 2019 (Schreiner et al., 2020). The C2 satellites are in low inclination orbits, providing observations over low latitudes out to ~40°N–S, with ~70% of the measurements over the deep tropics 20°N–S (see e.g., Figure 2 of Ho et al., 2020). We analyze C2 temperature profiles (so-called dry temperature retrievals, atmPrf) over altitudes 10–30 km sampled at 200 m vertical resolution for the period October 2019–April 2020, using data obtained from the COSMIC Data Analysis and Archive Center (CDACC) website https://cdaac-www.cosmic.ucar.edu/. Our focus is on the thermal variability in the UTLS region ~15–25 km. Stratospheric winds have a strong influence on UTLS equatorial waves (e.g., Kawatani et al., 2009; Kim et al., 2019), in particular wind variations tied to the QBO. During the period studied here the lower stratospheric equatorial zonal winds were evolving from weak westerly to weak easterly winds (~+5 to −5 m/s) over altitudes ~17–25 km, with stronger easterly winds above 25 km (see https://acd-ext.gsfc.nasa.gov/Data_services/met/qbo/qbo.html). Hence, the equatorial waves analyzed here are probably not strongly influenced by the background winds, at least below 25 km.

In order to study large-scale waves including extension to diurnal variability, we derive a 6-hourly gridded version of the C2 temperature data on a 4° latitude by 10° longitude (ϕ,λ) grid, using a Gaussian-weighted average (in longitude and time) of the individual GPS measurements, following Randel and Wu (2005). Gridded temperatures are calculated as T_{grid} (λ,t) = Σ w_i T_i/Σ w_i, with T_i the individual C2 measurements (within+/−2° of each grid latitude) and w_i = exp (−[($\Delta\lambda$/D)^2+(Δt/T)^2]) is a Gaussian weighting function in longitude and time. Here $\Delta\lambda$ is the difference between the grid center and each C2 measurement, Δt the corresponding time difference, using D = 2° and T = 1 h. The parameters D and T are empirically chosen to provide reasonable gridding and spectral analysis results, and this mapping provides a straightforward method to grid the irregular C2 data and smooth the grid over short data voids. As a note, Randel and Wu (2005) use D = 10° and T = 1 day, because the observations were more sparse in that study. Figure 1 shows an example of C2 sampling near the equator for one day (January 10, 2020), along with the resulting gridded temperature field. Results in Figure 1 highlight strong zonal temperature structure with patterns centered over the equator (e.g., the warm region near ~100°E), which is associated with an equatorial Kelvin wave that is known to dominate variability near the tropical tropopause (e.g., Kim & Son, 2012; Scherllin-Pirscher et al., 2017).

In order to identify coherent large-scale wave behavior we perform zonal wavenumber-frequency spectrum analysis of the gridded temperature data for the 120-day period December 1, 2019 to March 29, 2020 (with 4x daily time samples), using the standard formulation of Hayashi (1982). Following previous studies (e.g., Alexander et al., 2008; Kawatani et al., 2009; Wheeler & Kiladis, 1999) we analyze the gridded temperature wave structures that are symmetric (S) and antisymmetric (AS) about the equator as $T_S = (T(\phi) + T(-\phi))/2$ and T_{AS} = ($T(\phi)$−T ($-\phi$))/2, with averages over latitudes 16°N–S. We note that our results show actual

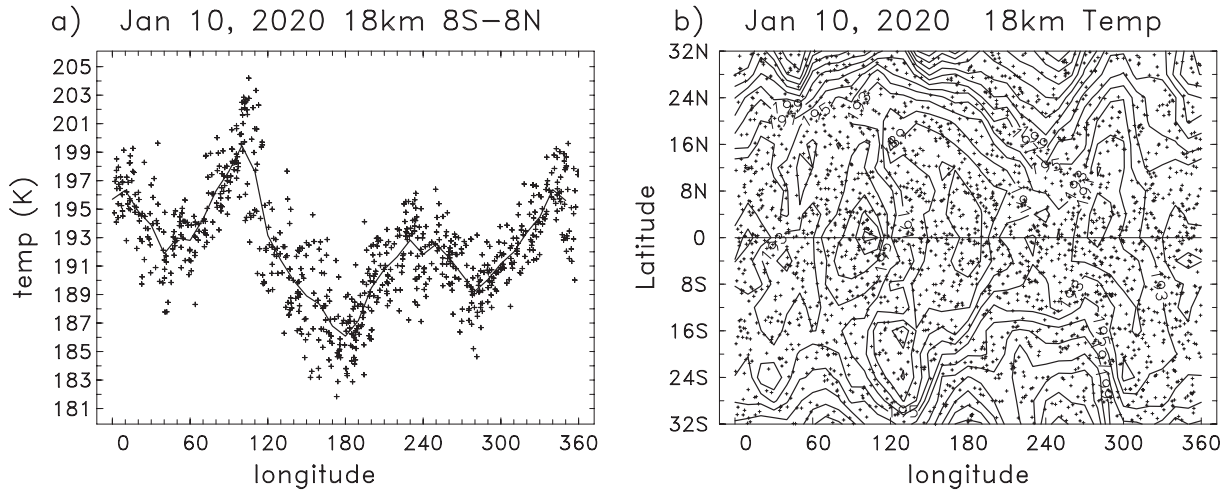

Figure 1. (a) Crosses indicate individual C2 temperature measurements at 18 km over 8°N–S for January 10, 2020. The thin line shows the gridded temperature field averaged over 8°N–S. (b) Gridded spatial structure of temperatures at 18 km on this day, with the crosses indicating the C2 measurement locations.

temperature wave power, not ratios of power compared to a smoothed background spectrum as in Wheeler and Kiladis (1999).

We also analyze the "residual" temperature, which is defined as the difference between the C2 profile measurements and the nearby gridded temperature fields, $T_{res} = T_i - T_{grid}$. For these calculations we take the daily average gridded values, and calculate daily average residual variances from measurements within the 4 ° × 10 ° latitude-longitude grid box. These differences represent small-scale or high frequency (below daily) variability that is not captured in the gridded temperature fields, possibly including gravity waves; the residuals include diurnal variance, but that is a small component. Examples of this variability are evident in Figure 1a as the differences between the individual data points and the gridded field. Similar analyses (differences from horizontally gridded fields) have been used to identify the statistical structure of small-scale gravity waves in RO data by for example, Schmidt et al., 2016, Wang & Alexander, 2010, and Xu et al., 2018.

We include some brief comparisons with observed infrared brightness temperature measurements as a proxy for tropical deep convection. The proxy is derived from the NCEP/CPC GMP MERGE_IR product (obtained from https://doi.org/10.5067/P4HZB9N27EKU), which consists in global (60°S–60°N) brightness temperature data in the infrared atmospheric window merged from the constellation of geostationary satellites (Janowiak et al., 2017). The original product is available at half-hourly, 4-km resolution; as a convective proxy, we chose the fraction of pixels with brightness temperature below 235 K within 1 h and in 1 by 1° grid boxes. The 235 K threshold was shown by Liu et al. (2007) to include both convective cores and the surrounding anvils and to match the pattern of deep convection, at least qualitatively.

3. Results

3.1. Resolved Equatorial Waves and Tides

Time series of daily zonal temperature variance at 18 km averaged over 8°N–S from C2 data are shown in Figure 2, including total variance calculated from the full individual C2 measurements ($\sigma^2_{total} = \Sigma (T_i - T_{bar})^2$), the gridded field ($\sigma^2_{grid} = \Sigma (T_{grid} - T_{bar})^2$) and the residual ($\sigma^2_{resid} = \sigma^2_{total} - \sigma^2_{grid}$). Here, T_{bar} is the zonal average and summations are appropriately weighted with the number of respective observations. Zonal temperature variance exhibits several maxima throughout the period, and the majority of the variance is captured by the gridded component, i.e. most of the temperature variability is associated with large-scale waves resolved by the 10° longitude grid. The zonal mean residual variance in Figure 2b is relatively constant in time, and is as energetic as the gridded field when the large-scale waves are quiescent. Further details of the residual are discussed below.

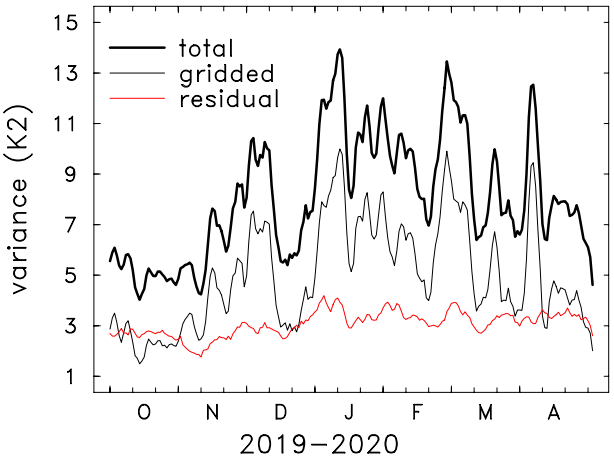

Figure 2. Time series of zonal temperature variance (K^2) at 18 km over 8°N–S, calculated from the full C2 measurements (total), from the gridded fields and the residual (difference between the total and gridded results).

As is well-known, the large-scale temperature fields in the tropical lower stratosphere are dominated by Kelvin waves (e.g., Alexander et al., 2008; Kim & Son, 2012; Scherllin-Pirscher et al., 2017). This behavior is characterized by eastward traveling planetary-scale waves with period near 20 days (zonal phase speeds ~ 20 m/s), as shown for the gridded C2 data at 18 km (~75 hPa) in Figure 3a. Interestingly, these waves show near-continuous propagation for more than three times around the globe starting in late-December. Quasi-stationary temperature anomalies are also observed near longitudes 180°–240° in Figure 3a, which are climatological features (e.g., Figure 4b of Scherllin-Pirscher et al., 2017). Snapshots of Kelvin wave vertical structure are analyzed further below, showing a characteristic eastward phase tilt with height and a typical vertical wavelength near ~6 km. Kelvin waves account for a majority of the gridded (and total) temperature variance throughout the season in Figure 2. Figure 3b shows longitude-time evolution of the residual temperature variance at 18 km, which will be discussed further in Section 3b.

Zonal wavenumber-frequency temperature power spectra for symmetric and antisymmetric equatorial temperatures at 20 km are shown in Figure 4, and similar spectra are found for altitudes from the tropopause throughout the lower stratosphere (~17–25 km). Spectra are shown for frequencies 0–1.3 cycles per day (cpd), as higher frequencies (out to 2.0 cpd) are poorly resolved in the 6-h grids. Symmetric power (Figure 4a) is dominated by eastward traveling Kelvin waves, with spectral peaks out to zonal wavenumber 4 and beyond, along with low frequency westward moving planetary-scale waves consistent with equatorial Rossby waves. Figure 4 includes theoretical equatorial wave dispersion curves (calculated for a motionless background flow) for several different equatorial wave modes and vertical wavelengths 4, 6, and 8 km, with labeling following standard nomenclature, e.g. Wheeler & Kiladis, 1999 (here, "n" is the meridional mode index). These wavelengths correspond to equivalent depths near 16, 37, and 66 m, respectively, with wavelengths calculated using a background stratospheric Brunt-Vaisala frequency squared value of $N^2 = 4*10^{-4}$ sec^{-2}. The theoretical dispersion curves show reasonable agreement with the observed power spectra. The

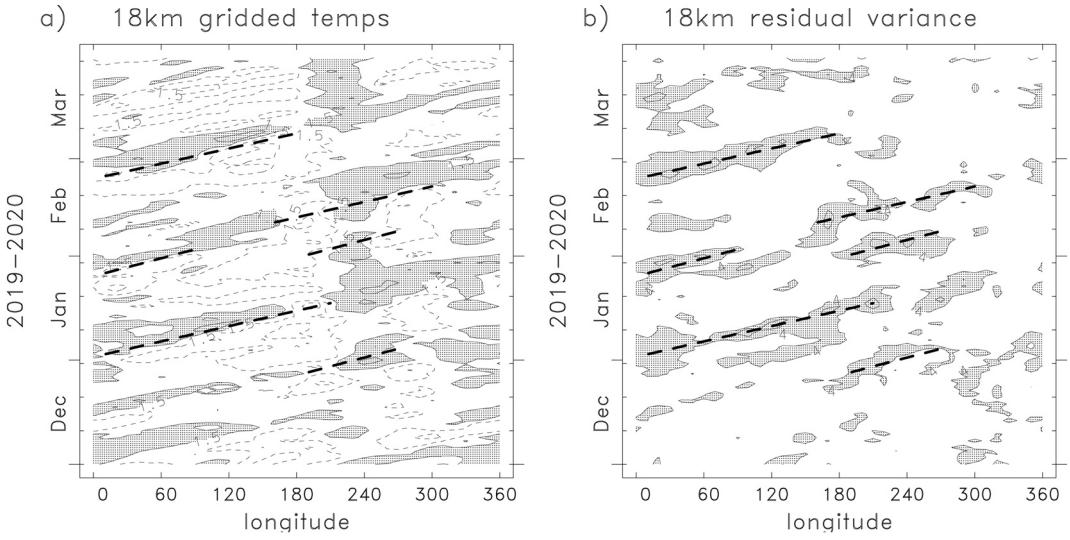

Figure 3. (a) Longitude-time diagram of gridded temperature anomalies over the equator (8°N–S) at 18 km (contours of+/−1.5, 4.5 K) highlighting eastward traveling Kelvin waves. (b) Residual temperature variance over 8°N–S at 18 km, with contour interval of 4 K^2. The thick dashed lines in (b) follow some of the residual variance maxima, and these are duplicated in (a) to show relation to the gridded temperatures. The small tick marks on the time axes denote 10-day intervals.

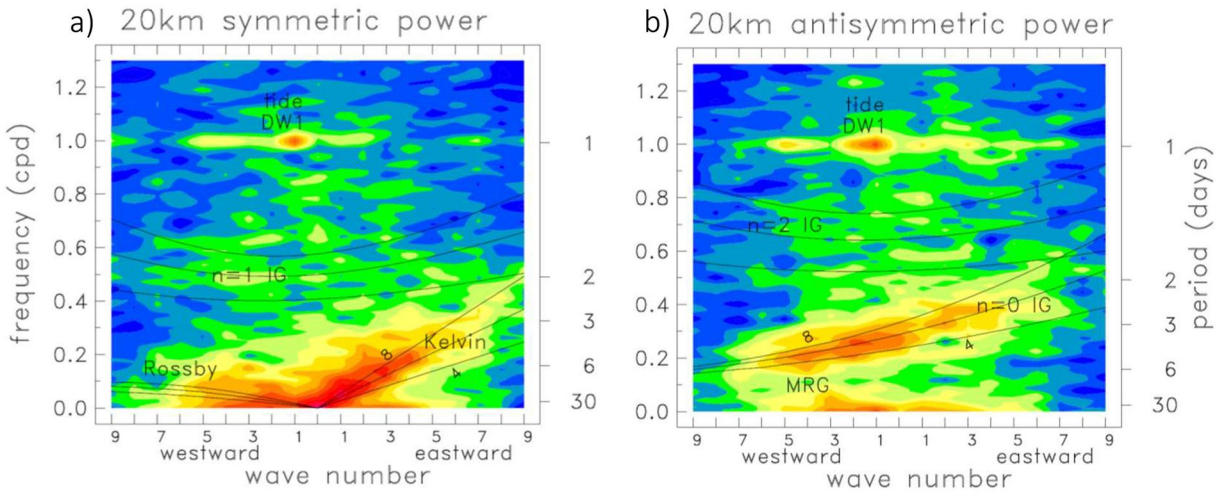

Figure 4. Zonal wavenumber-frequency power spectra at 20 km for (a) symmetric and (b) antisymmetric equatorial waves over 0–16°N–S, derived from gridded C2 data. The color scale is shown in Figure 5. The black lines denote equatorial wave dispersion curves for symmetric and antisymmetric waves, following for example, Wheeler & Kiladis, 1999. These are displayed for a set of vertical wavelengths 4, 6, and 8 km, corresponding to equivalent depths near 16, 37, and 66 m, as discussed in text. Labels indicate maxima associated with various wave modes, including equatorial Rossby, Kelvin, mixed Rossby-gravity (MRG), inertia-gravity (IG) waves and migrating diurnal tide (DW1).

symmetric spectrum (Figure 4a) also shows a weak maximum for westward moving waves with period ~2 days, consistent with higher order $n = 1$ inertia gravity (IG) waves.

The antisymmetric power spectrum (Figure 4b) show peaks for westward moving waves ~1–5 with periods ~4–6 days, linked to mixed Rossby-gravity (MRG) waves, along with higher frequency (~2.5–4 days) eastward traveling planetary scales ($n = 0$ IG waves). These antisymmetric temperature waves are consistent with previous observations in the lower stratosphere, for example, Alexander et al., 2008; Alexander & Ortland, 2010, Kiladis et al., 2016, and the maxima are especially distinct in the spectra derived from high density C2 measurements. The observed spectrum in Figure 4b agrees best with the theoretical dispersion curves for vertical wavelengths ~6 km.

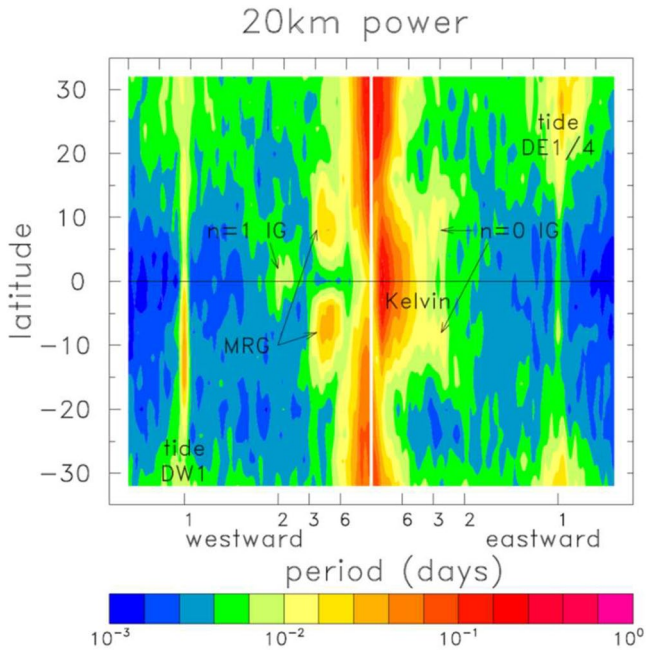

Figure 5. (a) Eastward-westward power spectra at 20 km as a function of latitude for combined zonal waves 1–6. Labels indicate various equatorial modes, as in Figure 4.

Both the symmetric and antisymmetric spectra in Figure 4 show a diurnal peak (frequency near 1.0 cpd) for westward moving zonal wave 1, which is the well-known migrating (or sun-synchronous) diurnal tide (so-called DW1). The migrating diurnal tide has been isolated in multi-year records of radio occultation measurements by Das et al. (2020), Zeng et al. (2008), Pirscher et al. (2010), and Xie et al. (2010) and shows up clearly in this relatively short record from C2. Amplitude and phase structure of the diurnal tide is discussed below. In the lower stratosphere the DW1 amplitude is maximum over ~20°S to 0° (during this boreal winter season), with a resulting projection onto symmetric and antisymmetric components in Figure 4.

Latitudinal structure of the various equatorial wave modes is illustrated for the 20 km level in Figure 5, combining power from zonal wavenumbers 1–6. Similar patterns are found at all levels throughout the lower stratosphere. The eastward Kelvin wave dominates power near the equator, with a symmetric maximum over ~10°N–S. Westward MRG waves show distinctive ~4–6 day period maxima near ~8°N and S which are out of phase (antisymmetric). Weaker but identifiable antisymmetric maxima are also seen for $n = 0$ eastward IG waves near ~3 day period, along with a symmetric $n = 1$ westward peak over the equator near 2 days period. Vertical structure of the symmetric and antisymmetric power for combined wavenumbers 1–6 (Figures 6a and 6b) reveal each of the

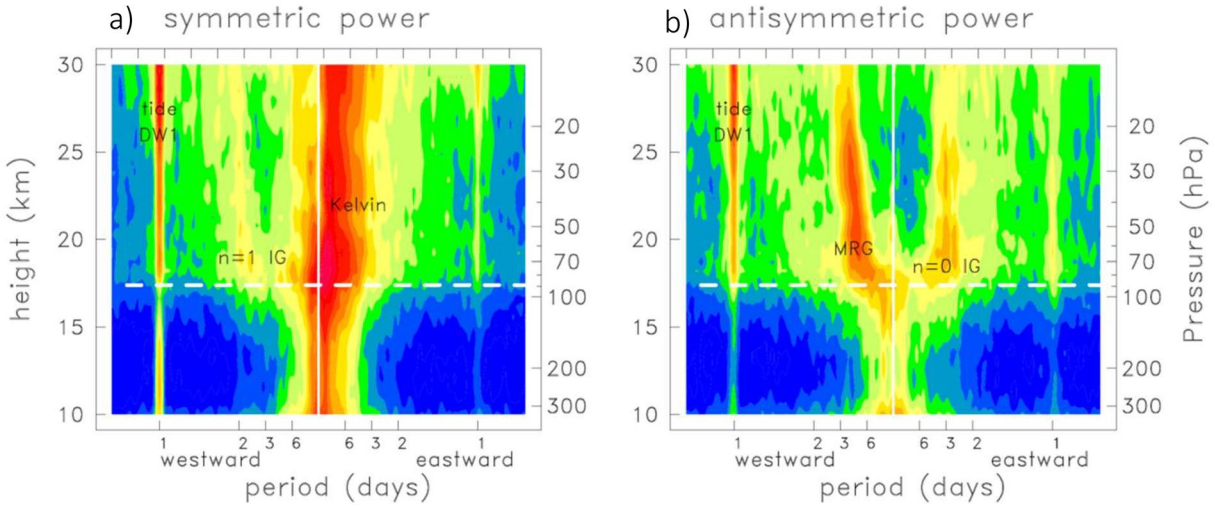

Figure 6. Height versus frequency power spectra for combined zonal waves 1–6, for (a) symmetric and (b) antisymmetric components. Labels indicate various wave modes, as in Figures 4 and 5. The white dashed lines indicate the tropopause altitude. The color scale is the same as in Figure 5.

spectral peaks discussed above, and show that the waves extend from approximately the tropopause (17 km) to above 25 km, and to higher altitudes for the Kelvin waves and DW1 tide. The MRG waves in Figure 6b show a systematic shift to higher frequencies at higher altitude (also seen for the $n = 1$ IG mode), and this behavior is consistent with dissipation of lower frequencies (slower phase speeds) as the waves propagate vertically from the tropopause level through weak zonal mean winds associated with the QBO. Another feature seen in Figure 6 is the sudden shift to lower periods that occurs immediately below the tropopause, indicative of the slower phase speeds of convectively coupled modes versus the dry stratospheric modes, as expected from theory and other observational studies (e.g., Kiladis et al., 2009).

In addition to the westward DW1 diurnal tide, Figure 5 furthermore reveals spectral peaks for *eastward* propagating diurnal oscillations at latitudes poleward of ~15°N and S. These are associated with non-migrating tides with maxima for zonal wavenumbers 1–4 in the C2 data, although we note larger uncertainty for spectrum analysis of diurnal oscillations from C2 data at extratropical latitudes because of fewer observations. We term this the DE1/4 mode in analogy to the non-migrating eastward zonal wave 3 mode (DE3) often observed in the middle atmosphere (e.g., Forbes et al., 2006). The eastward non-migrating tides are likely forced by the diurnal cycle of spatially fixed convective heating in the tropical troposphere (Hagan & Forbes, 2002); the DE3 tidal oscillations propagate vertically and reach large amplitudes in the mesosphere and lower thermosphere, and feature prominently in coupling the lower and upper atmosphere (e.g., Forbes et al., 2006).

Spatial structure of the rms amplitudes of DW1 and DE1/4 derived from C2 data are shown in Figure 7, with rms amplitudes defined as $A_{rms} = (2{*}T_{var})^{1/2}$, with temperature variance T_{var} calculated as spectral power integrated over frequencies 0.9–1.1 cpd, for westward zonal wave 1 (DW1) and eastward zonal waves 1–4 (DE1/4). Amplitude of DW1 (Figure 7a) is similar to that shown in Zeng et al. (2008), with maximum centered in low latitudes increasing in amplitude from ~0.2 K near the tropopause to ~ 0.5 K at 30 km. The corresponding phase (not shown) shows regular downward progression from 30 km to the tropopause level, for example, Zeng et al., 2008, their Figure 5b.

The structure of diurnal variability near and above the tropical tropopause has interesting spatial structure related to the diurnal cycles of continental convection. This behavior is shown in Figure 8a, isolating the average diurnal cycle at each longitude at 19 km for data averaged over 0–16°S. These results highlight a clear westward propagating planetary wave pattern with amplitude ~ 0.2 K, modulated by enhanced local temperature maxima over continental regions with strong diurnal convection (Africa and South America). This diurnal behavior of deep convection is shown in Figure 8b (for data similarly averaged over 0–16°S), illustrating the hourly variability from the infrared brightness convective proxy. Temperature anomalies in Figure 8a are strongest over Africa (where the strongest and deepest convection occurs, Zipser et al., 2006),

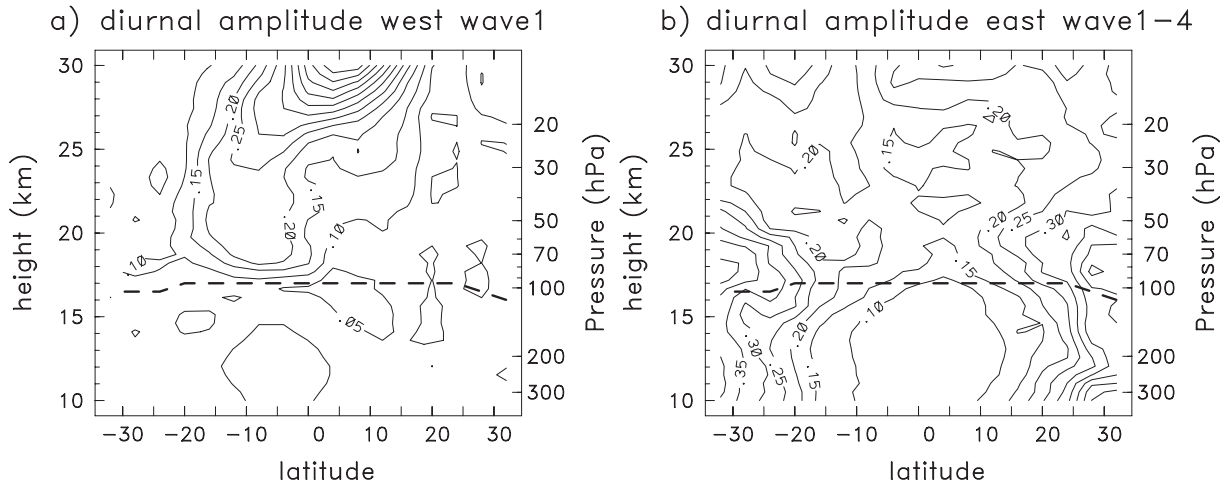

Figure 7. Meridional cross sections of rms amplitude for (a) migrating diurnal tide DW1, and (b) non-migrating diurnal tide DE1/4 (discussed in text). Contour interval is 0.05 (K) The dark dashed line is the thermal tropopause.

with local maxima up to+/−0.8 K. The phasing is such that coldest lower stratosphere temperatures occur centered near ~6 p.m. local time, near the late afternoon maxima in continental deep convection seen in Figure 8b (e.g., Liu & Zipser, 2008). This local temperature behavior in the lower stratosphere in response to diurnal convection has been studied by Khaykin et al. (2013), who isolated the signals from radio occultation

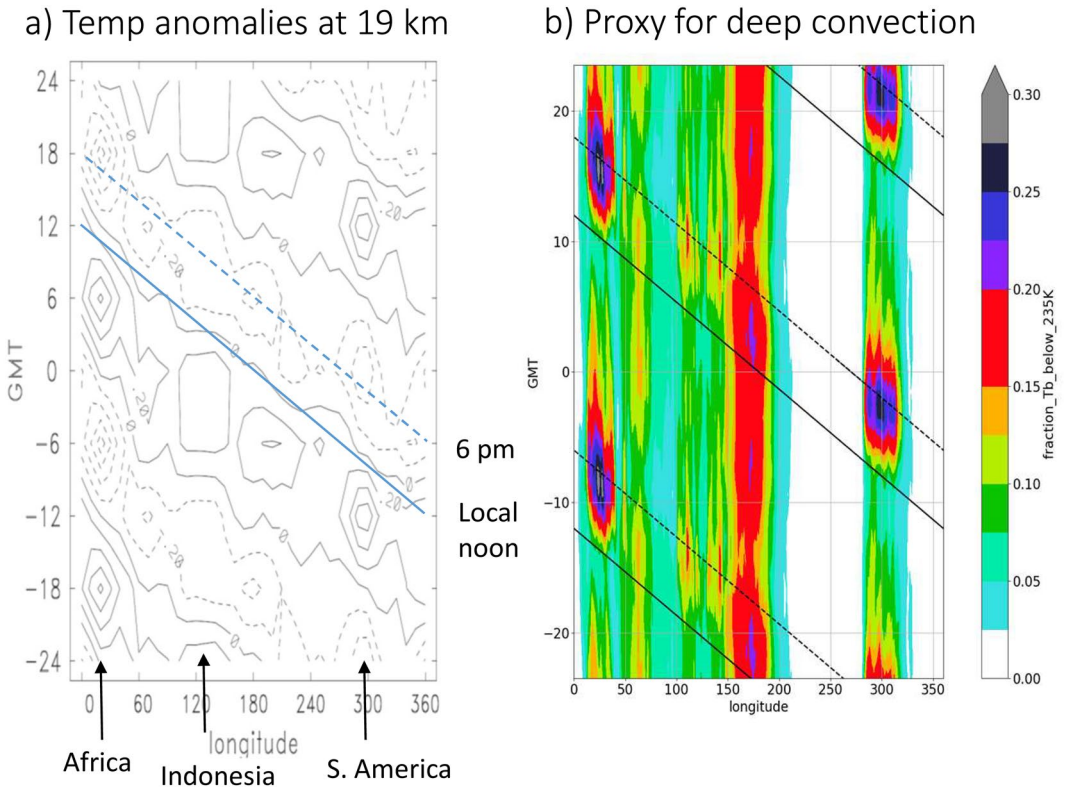

Figure 8. (a) Diurnal cycle of temperature at 19 km as a function of longitude, for C2 data averaged over latitudes 0–16°S. The diurnal cycle (departure from the daily average) is repeated twice for clarity. Contour interval is 0.2 K, and the diagonal lines denote local noon and 6 p.m. (b) Hourly variations in fractional infrared brightness temperature below 235 K as a function of longitude, as a proxy for deep convection. These calculations also represent statistics over 0–16°S.

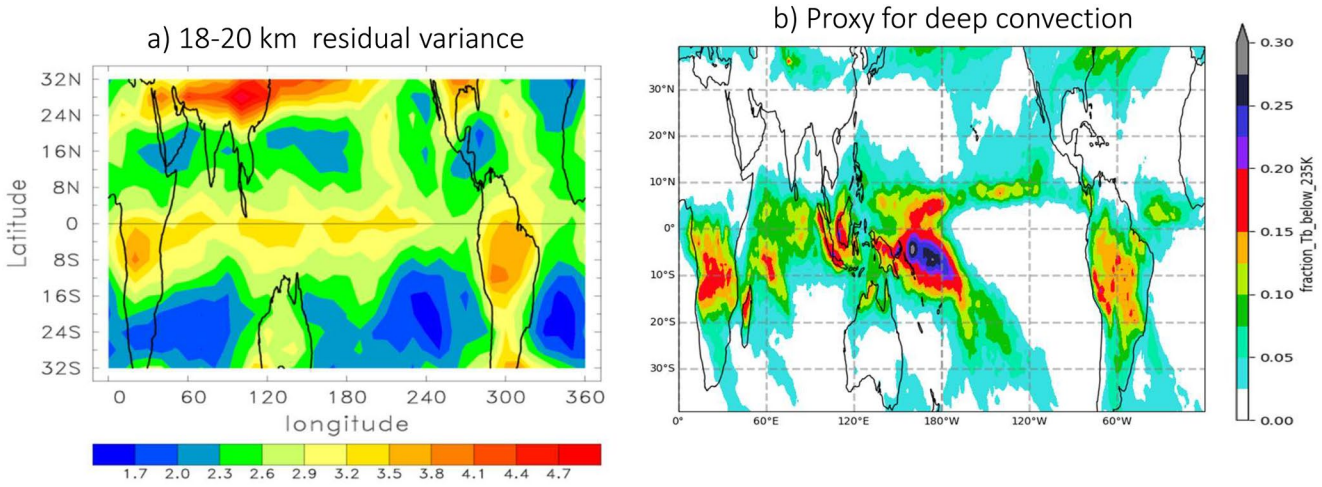

Figure 9. (a) Time average (December–February) residual temperature variance (K^2) for the 18–20 km layer. (b) Fraction of infrared brightness temperature below 235K for statistics over the same period, which is a proxy for tropical deep convection.

data according to land and ocean regions. The patterns of localized lower stratosphere cooling associated with tropical deep convection are similar to behavior noted by Paulik and Birner (2012), Kim et al. (2018) and Johnston et al. (2018), all based on radio occultation temperature measurements. Although not shown here, C2 data reveal out-of-phase diurnal temperature variations in the upper troposphere (10–14 km) that are approximately half as large as the lower stratosphere patterns in Figure 8a.

Spatial structure of the eastward DE1/4 tide (Figure 7b) is very different from DW1, with temperature amplitudes of ~0.3-0.4 K polewards of ~15°N and S, and maxima over ~15–20 km and also below ~12 km. Cross-spectrum analysis reveals that the extratropical maxima for individual waves 1–3 are statistically coherent and out-of-phase between hemispheres (not shown).

3.2. Residual Temperature Variance

The residual temperature variance represents small scales that are below the 10° longitude and 6-h time resolutions of the gridded fields, and we examine space-time structure by calculating the variance of the C2 residuals within each 4 ° × 10 ° grid box, calculated for daily samples. The time average (December 2019–February 2020) residual variance for the 18–20 km layer is shown in Figure 9a, revealing localized spatial maxima. In the deep tropics, residual variance shows isolated maxima over Africa and S. America (~16°S to 0°) that are likely associated with small-scale gravity waves forced by the underlying frequent continental convection, as indicated in Figure 9b. Small fractions of these variance maxima (~0.4 K^2) are due to local diurnal variations discussed above in relation to Figure 8a. These relative maxima may reflect the higher and more penetrating convection observed over tropical continental regions, for example, Liu & Zipser, 2005. Figure 9a also shows a broad longitudinal maximum in variance near the equator over the Indian and Pacific oceans that could be linked with underlying low latitude convection (which is mainly south of the equator in Figure 9b) and/or structures in the large-scale flow, as explored further below. The residual temperature variance in Figure 9a furthermore shows maxima over continental regions in the extratropics, including a large maximum over and downstream of Asia and over North America. These could possibly be related to gravity waves in the lower stratosphere generated by flow over topography, for example, Wang & Geller, 2003. There are also maxima in the Southern Hemisphere over Australia and over the Andes (~300°), and the latter is a well-known hot spot for stratospheric gravity wave activity, e.g. Eckerman & Preusse, 1999. The presence of coherent spatial structures in the time average statistics in Figure 9 argues that the temperature residuals calculated in a simple manner from C2 data represent actual geophysical variability.

Space-time variations of residual variance in the tropical UTLS furthermore shows coherence with the large-scale Kelvin waves. Figure 3b shows the residual variance over the equator at 18 km as a function of

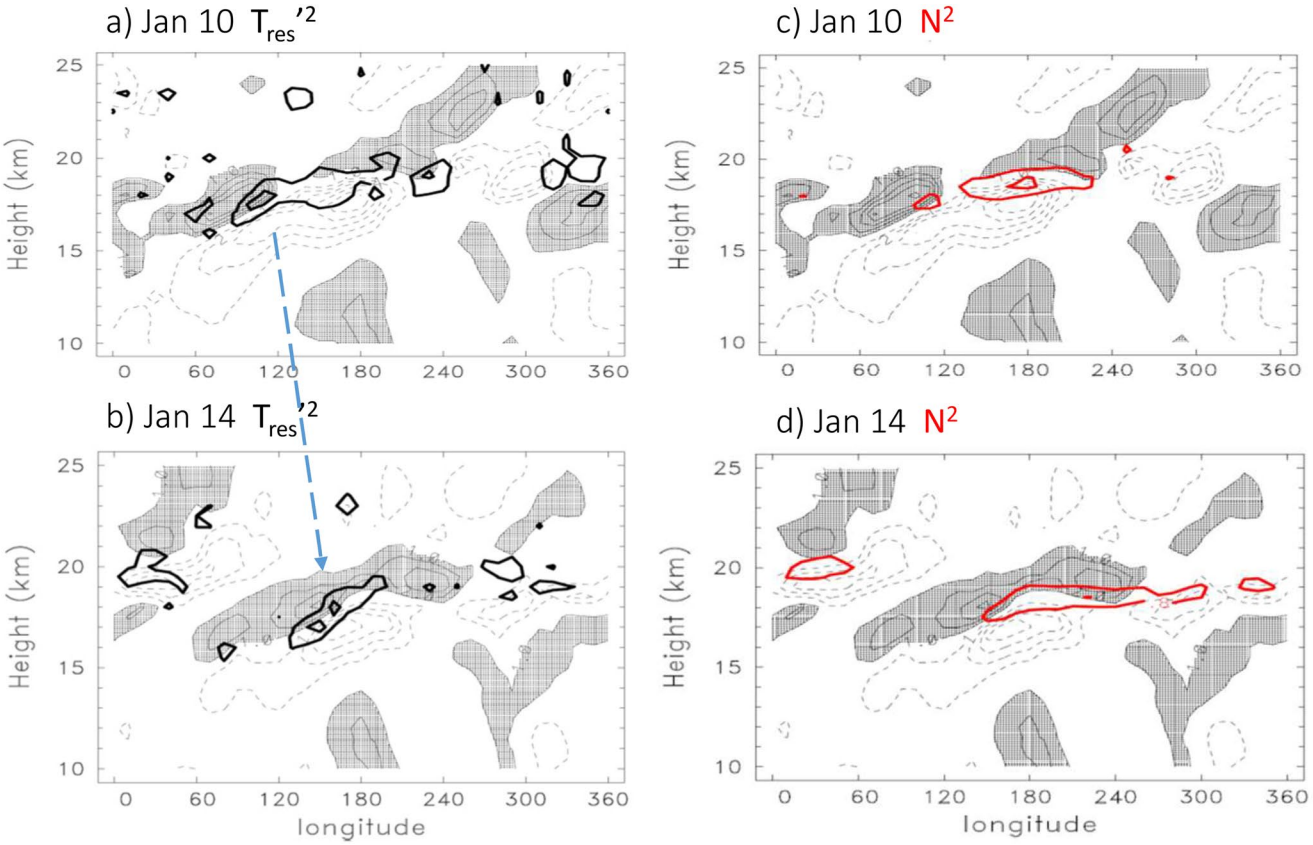

Figure 10. (a–b) Cross sections showing the relationship of small-scale residual temperature variance averaged over 8°N–S (dark lines with contour interval of 4 K^2) with large-scale "background" gridded temperature anomalies (light lines, contours of+/−1,2,3,...K), which are primarily associated with eastward propagating Kelvin waves. Snapshots are shown for January 10 and 14, 2020 (c–d) Red lines indicate regions of enhanced Brunt-Vaisala frequency squared (N^2, contours of 8 and $10*10^{-4}$ sec^{-2}) for these days, together with the background gridded temperatures (the same as in the left panels). Residual variance maxima are sandwiched between strong gradients in the background fields in regions of enhanced N^2, and follow the eastward phase progression.

longitude and time, highlighting episodic eastward traveling maxima that are closely related to the "background" large-scale Kelvin waves in Figure 3a. Dashed lines in Figures 3a–3b show that localized residual variance maxima occur in the longitudinal gradient zones of the background Kelvin wave temperatures; maxima also occur with respect to vertical temperature gradients for Kelvin waves. The spatial relationships between the residual variance and the gridded temperature anomalies, and their evolution for several example days in January are shown in Figures 10a and 10b. These examples show residual variance maxima sandwiched between large positive and negative temperature patterns associated with Kelvin waves, with the enhanced residuals following the eastward slope with altitude and phase progression with time. The background Kelvin waves have a vertical wavelength of ~6 km, consistent with Figure 4, while the residual variance typically has a narrower vertical scale of 1–2 km. An example of this enhanced variability is seen in the individual C2 measurements over longitudes ~140–170°E in Figure 1a, for the same day as in Figure 10a.

The fact that strong residual variance occurs in the longitudinal shear zones of Kelvin waves could partly reflect fitting sharp zonal gradients in the C2 data on a 10° longitude grid. However, there is also a plausible physical explanation attributing the variability to enhancement of ubiquitous gravity waves in the lower stratosphere. A possible interpretation is that the small-scale residual variance ($T_{res}'^2$) is responding to local variations in background static stability (N^2) associated with the large-scale Kelvin waves (N is the Brunt-Vaisala frequency). Figures 10c and 10d show that positive stability (N^2) anomalies occur in the regions of enhanced dT/dz associated with the Kelvin waves, spatially co-located near regions of enhanced $T_{res}'^2$. This relationship can be expected for gravity wave temperature amplitudes propagating vertically without dissipation in a varying background flow, where the temperature variance ($T_{res}'^2$) is proportional to

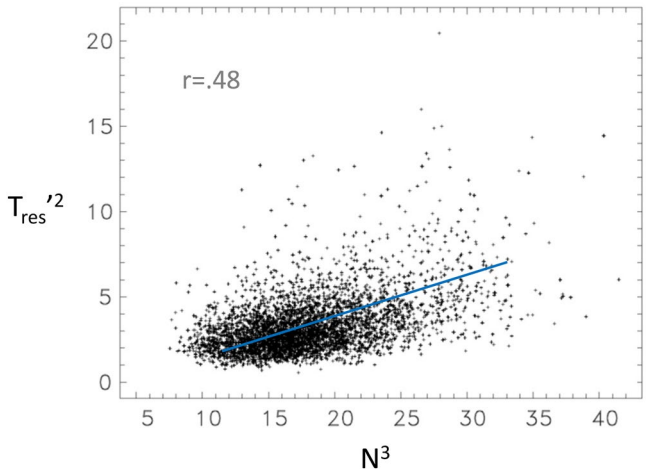

Figure 11. Scatter plot of 18 km residual variance $T_{res}'^2$ (K^2) over the equator versus co-located N^3 (10^{-6} sec^{-3}), including data from 36 longitudes for all days during December 2019–March 2020. Data are daily averages over 8°N–S.

background N^3 (Fritts & Alexander, 2003, Equation 55). Figure 11 shows the statistical relationship between $T_{res}'^2$ and N^3 at 18 km including data averaged over 8°N–S for all longitudes during December–March, and while the relationship is not compact there is a clear tendency for largest residuals to be related to largest N^3. This is consistent with a partial explanation of $T_{res}'^2$ in this region as enhanced gravity wave variance.

4. Summary and Discussion

The concentrated space-time sampling of high vertical resolution temperature retrievals from C2 allows the novel generation of a 6-hourly gridded temperature data set over low latitudes, allowing analysis of large- and small-scale temperature variability in the tropical UTLS. The large-scale gridded results from C2 show the well-known dominance of eastward moving planetary-scale Kelvin waves with periods near 20 days, in addition to strong westward traveling MRG waves (zonal waves ~1–5, periods ~4–6 days). The MRG waves have smaller (antisymmetric) tropical temperature amplitudes than the symmetric Kelvin waves, but are important for equatorial meridional wind and westward momentum fluxes into the lower stratosphere (e.g., Kim et al., 2019). The C2 data also show evidence for smaller amplitude inertia-gravity waves, both eastward and westward modes with ~2–3 days period and distinctive meridional structures, which are interesting but less important for upward momentum fluxes (Kawatani et al., 2010). Our analyses reveal the westward migrating zonal wave 1 diurnal tide (DW1) with maximum amplitude in the tropical stratosphere, as found in previous studies with RO data (e.g., Zeng et al., 2008). The tropical diurnal variations have local maxima above the tropopause embedded within the planetary DW1 mode linked to strong continental convection, with cooling tied to late afternoon convection; these local patterns are strongest over Africa (Figure 8a). This result is a complement to the land-ocean diurnal separation used in Khaykin et al. (2013). A new finding here is enhanced power for eastward non-migrating diurnal tides at extratropical latitudes in the troposphere and lower stratosphere of both hemispheres (Figures 5 and 7b), with the majority of power at zonal waves 1–4 (DE1/4). The C2 sampling does not allow characterization of this behavior at higher latitudes, but that might be achieved in the future by combining RO measurements from additional satellites. As a note, there are numerous other studies of tides in the stratosphere and higher altitudes based on satellite observations (e.g., Mukhtarov et al., 2009; Pancheva et al., 2010; Sakazaki et al., 2015, 2018; Wu et al., 1998; Zhang et al., 2010), but these typically highlight behavior above the middle stratosphere (~30 km). The radio occultation measurements provide a complementary data source at lower altitudes, as used by Sakazaki et al., 2015.

We have also explored the systematic behavior of small-scale ("residual") temperature variances ($T_{res}'^2$) in C2 measurements, based on subtracting the large-scale gridded temperature field. Part of these residuals could be associated with limited grid resolution and C2 data sampling, but the patterns of residual variance are suggestive of geophysical behavior tied to small-scale gravity waves. As noted above, our separation of small scales based on differences with horizontal gridded fields is similar to previous studies (e.g., Wang & Alexander, 2010), and is a complement to separation based on filtering vertical profiles. Time averages in the lower stratosphere (Figure 9a) show $T_{res}'^2$ maxima over Africa and South America that are consistent with forcing from frequent tropical convection, in addition to maxima over midlatitude continents that may be linked to orography and/or convective sources. Further studies of the detailed time variability in these regions may be interesting. Lower stratosphere residuals also maximize over the equatorial Indian and Pacific oceans, and here the small-scale variance is organized in regions linked to traveling shear zones of the background large-scale Kelvin waves (Figures 3 and 10). We speculate that this behavior can be partly explained by variations in background stability (N^2), which maximize in narrow vertical layers tied to the Kelvin wave vertical structure and are approximately co-located with $T_{res}'^2$ (Figure 10). A theoretical expectation of this relationship is that $T_{res}'^2$ is proportional N^3, and some evidence for this behavior is found in the C2 data statistics (Figure 11). We note that while this is one plausible physical explanation, there are other

mechanisms that could contribute to linking small-scale temperature variances with Kelvin waves, such as shear instabilities (Flannaghan & Fueglistaler, 2011; Fujiwara et al., 2003). This is unlikely here, since for Kelvin waves shear anomalies are minimum where stability (N^2) is maximum.

Our analyses have shown a snapshot of equatorial wave variability for the first several months of C2 observations, and it will be interesting to extend analyses to longer time periods to quantify links to tropospheric forcing and sensitivity to background stratospheric winds. These direct observations are useful for detailed comparisons to meteorological reanalyzes (especially before the assimilation of C2 data); the C2 data are now being assimilated into the major meteorological centers for analyses, forecasting and reanalyzes (e.g., Healy, 2020). The C2 data can also be useful for evaluating wave behavior in high resolution global model simulations (e.g., Holt et al., 2020). As a note, the time period analyzed here also overlaps the recent Strateole2 long-duration balloon measurements made in the tropical lower stratosphere during November 2019–February 2020 (https://webstr2.lmd.polytechnique.fr/#/), and the C2 observations may be useful to provide a global context to the high resolution balloon measurements.

Data Availability Statement

COSMIC-2 data were obtained from the COSMIC Data Analysis and Archive Center (CDACC) website https://cdaac-www.cosmic.ucar.edu/. The deep convective proxy brightness temperature data were obtained from https://doi.org/10.5067/P4HZB9N27EKU.

Acknowledgments
The National Center for Atmospheric Research is sponsored by the U.S. National Science Foundation. This work has been partially supported by the COSMIC NSF-NASA Cooperative Agreement under Grant 1522830. The authors thank Rolando Garcia, Joan Alexander, Rick Anthes, Ben Johnston, and Janet Zeng for discussions and comments on the manuscript. George Kiladis and another anonymous reviewer provided knowledgeable and constructive reviews that substantially improved the paper.

References

Alexander, M. J., & Ortland, D. A. (2010). Equatorial waves in High Resolution Dynamics Limb Sounder (HIRDLS) data. *Journal of Geophysical Research*, *115*(D24111). https://doi.org/10.1029/2010JD014782

Alexander, S. P., Tsuda, T., Kawatani, Y., & Takahashi, M. (2008). Global distribution of atmospheric waves in the equatorial upper troposphere and lower stratosphere: COSMIC observations of wave mean flow interactions. *Journal of Geophysical Research*, *113*(D24). D24115. https://doi.org/10.1029/2008JD010039

Chang, K.-W., & L'Ecuyer, T. (2020). Influence of gravity wave temperature anomalies and their vertical gradients on cirrus clouds in the tropical tropopause layer - A satellite-based view. *Atmospheric Chemistry and Physics*, *20*, 12499–12514. https://doi.org/10.5194/acp-20-12499-2020

Das, U., Ward, W. E., Pan, C. J., & Das, S. K. (2020). Migrating and non-migrating tides observed in the stratosphere from FORMOSAT-3/COSMIC temperature retrievals. *Annales Geophysicae*, *38*, 421–435. https://doi.org/10.5194/angeo-38-421-2020

Eckerman, S. D., & Preusse, P. (1999). Global measurements of stratospheric mountain waves from space. *Science*, *286*, 1534–1537. https://doi.org/10.1126/science.286.5444.1534

Ern, M., Preusse, P., Krebsbach, M., Mlynczak, M. G., & Russell, J. M., III (2008). Equatorial wave analysis from SABER and ECMWF temperatures. *Atmospheric Chemistry and Physics*, *8*(4), 845–869. https://doi.org/10.5194/acp-8-845-2008

Flannaghan, T. J., & Fueglistaler, S. (2011). Kelvin waves and shear-flow turbulent mixing in the TTL in (re-)analysis data. *Geophysical Research Letters*, *38*(2). https://doi.org/10.1029/2010gl045524

Forbes, J. M., Russell, J., Miyahara, S., Zhang, X., Palo, S., Mlynczak, M., et al. (2006). Troposphere-thermosphere tidal coupling as measured by the SABER instrument on TIMED during July-September 2002. *Journal of Geophysical Research*, *111*, A10S06. https://doi.org/10.1029/2005JA011492

Fritts, D. C., & Alexander, M. J. (2003). Gravity wave dynamics and effects in the middle atmosphere. *Reviews of Geophysics*, *41*(1), 1003. https://doi.org/10.1029/2001RG000106

Fujiwara, M., Hasebe, F., Shiotani, M., Nishi, N., Vömel, H., & Oltmans, S. J. (2001). Water vapor control at the tropopause by equatorial Kelvin waves observed over the Galápagos. *Geophysical Research Letters*, *28*(16), 3143–3146. https://doi.org/10.1029/2001gl013310

Fujiwara, M., Iwasaki, S., Shimizu, A., Inai, Y., Shiotani, M., Hasebe, F., et al. (2009). Cirrus observations in the tropical tropopause layer over the western Pacific. *Journal of Geophysical Research*, *114*.D09304. https://doi.org/10.1029/2008JD011040

Fujiwara, M., Yamamoto, M. K., Hashiguchi, H., Horinouchi, T., & Fukao, S. (2003). Turbulence at the tropopause due to breaking Kelvin waves observed by the equatorial atmosphere radar. *Geophysical Research Letters*, *30*(4), 1171. https://doi.org/10.1029/2002GL016278

Hagan, M. E., & Forbes, J. M. (2002). Migrating and nonmigrating diurnal tides in the middle and upper atmosphere excited by tropospheric latent heat release. *Journal of Geophysical Research*, *107*(D24), 4754. https://doi.org/10.1029/2001JD001236

Hayashi, Y. (1982). Space-time spectral analysis and its applications to atmospheric waves. *Journal of the Meteorological Society of Japan*, *60*(1), 156–171. https://doi.org/10.2151/jmsj1965.60.1_156

Healy, S. (2020). ECMWF starts assimilating COSMIC-2 data. *ECMWF Newsletter*, *163*. https://www.ecmwf.int/en/newsletter/163/news/ecmwf-starts-assimilating-cosmic-2-data

Ho, S.-P., Shao, X. X., Zhang, B., Adhikari, L., Kireev, S., He, Y., et al. (2020). Initial Assessment of the COSMIC-2/FORMOSAT-7 Neutral Atmosphere Data Quality in NESDIS/STAR using in situ and satellite data. *Remote Sensing*, *12*, 4099. https://doi.org/10.3390/rs12244099

Holt, L. A., Alexander, M. J., Coy, L., Molod, A., Putman, W., & Pawson, S. (2016). Tropical waves and the quasi-biennial oscillation in a 7-km global climate simulation. *Journal of the Atmospheric Sciences*, *73*(9), 3771. https://doi.org/10.1175/JAS-D-15-0350.1

Holt, L. A., Lott, F., Garcia, R. R., Kiladis, G. N., Cheng, Y. M., Anstey, J. A., et al. (2020). An evaluation of tropical waves and wave forcing of the QBO in the QBOi models. *Quarterly Journal of the Royal Meteorological Society*. (In Press). https://doi.org/10.1002/qj.3827

Janowiak, J., Joyce, B., & Xie, P. (2017). NCEP/CPC L3 Half Hourly 4km Global (60S - 60N) Merged IR V1. In A. Savtchenko, & M. D. Greenbelt (Eds.), *Goddard Earth sciences data and information services center (GES DISC)*. https://doi.org/10.5067/P4HZB9N27EKU Accessed: 02/15/2020

Jensen, E., & Pfister, L. (2004). Transport and freeze-drying in the tropical tropopause layer. *Journal of Geophysical Research*, *109*, D02207. https://doi.org/10.1029/2003JD004022

Johnston, B. R., Xie, F., & Liu, C. (2018). The effects of deep convection on regional temperature structure in the tropical upper troposphere and lower stratosphere. *Journal of Geophysical Research - D: Atmospheres*, *123*(3), 1585–1603. https://doi.org/10.1002/2017jd027120

Kawatani, Y., Takahashi, M., Sato, K., Alexander, S. P., & Tsuda, T. (2009). Global distribution of atmospheric waves in the equatorial upper troposphere and lower stratosphere: AGCM simulation of sources and propagation. *Journal of Geophysical Research*, *114*, D01102. https://doi.org/10.1029/2008JD010374

Kawatani, Y., Watanabe, S., Sato, K., Dunkerton, T. J., Miyahara, S., & Takahashi, M. (2010). The roles of equatorial trapped waves and internal inertia-gravity waves in driving the quasi-biennial oscillation. Part I: Zonal mean wave forcing. *Journal of the Atmospheric Sciences*, *67*, 963–980. https://doi.org/10.1175/2009jas3222.1

Khaykin, S. M., Pommereau, J.-P., & Hauchecorne, A. (2013). Impact of land convection on temperature diurnal variation in the tropical lower stratosphere inferred from COSMIC GPS radio occultations. *Atmospheric Chemistry and Physics*, *13*, 6391–6402. https://doi.org/10.5194/acp-13-6391-2013

Kiladis, G. N., Dias, J., & Gehne, M. (2016). The relationship between equatorial mixed rossby-gravity and eastward inertio-gravity waves. Part I. *Journal of the Atmospheric Sciences*, *73*, 2123–2145. https://doi.org/10.1175/jas-d-15-0230.1

Kiladis, G. N., Wheeler, M. C., Haertel, P. T., Straub, K. H., & Roundy, P. E. (2009). Convectively coupled equatorial waves. *Reviews of Geophysics*, *47*.RG2003. https://doi.org/10.1029/2008RG000266

Kim, J., Randel, W. J., & Birner, T. (2018). Convectively driven tropopause-level cooling and its influences on stratospheric moisture. *Journal of Geophysical Research - D: Atmospheres*, *123*(1), 590–606. https://doi.org/10.1002/2017jd027080

Kim, J., & Son, S.-W. (2012). Tropical cold-point tropopause: Climatology, seasonal cycle, and intraseasonal variability derived from COSMIC GPS radio occultation measurements. *Journal of Climate*, *25*(15), 5343–5360. https://doi.org/10.1175/JCLI-D-11-00554.1

Kim, J.-E., Alexander, M. J., Bui, T. P., Dean-Day, J. M., Lawson, R. P., Woods, S., et al. (2016). Ubiquitous influence of waves on tropical high cirrus clouds. *Geophysical Research Letters*, *43*, 5895–5901. https://doi.org/10.1002/2016GL069293

Kim, Y.-H., Kiladis, G. N., Albers, J. R., Dias, J., Fujiwara, M., Anstey, J. A., et al. (2019). Comparison of equatorial wave activity in the tropical tropopause layer and stratosphere represented in reanalyzes. *Atmospheric Chemistry and Physics*, *19*, 10027–10050. https://doi.org/10.5194/acp-19-10027-2019

Liu, C., & Zipser, E. J. (2005). Global distribution of convection penetrating the tropical tropopause. *Journal of Geophysical Research*, *110*. D23104. https://doi.org/10.1029/2005JD006063

Liu, C., & Zipser, E. J. (2008). Diurnal cycles of precipitation, clouds, and lightning in the tropics from 9 years of TRMM observations. *Geophysical Research Letters*, *35*.L04819. https://doi.org/10.1029/2007GL032437

Liu, C., Zipser, E. J., & Nesbitt, S. W. (2007). Global distribution of tropical deep convection: Different perspectives from TRMM infrared and radar data. *Journal of Climate*, *20*(3), 489–503. https://doi.org/10.1175/jcli4023.1

Mote, P. W., & Dunkerton, T. J. (2004). Kelvin wave signatures in stratospheric trace constituents. *Journal of Geophysical Research*, *109*. D03101. https://doi.org/10.1029/2002JD003370

Mukhtarov, P., Pancheva, D., & Andonov, B. (2009). Global structure and seasonal and interannual variability of the migrating diurnal tide seen in the SABER/TIMED temperatures between 20 and 120 km. *Journal of Geophysical Research*, *114*.A02309. https://doi.org/10.1029/2008JA013759

Pancheva, D., Mukhtarov, P., & Andonov, B. (2010). Global structure, seasonal and interannual variability of the eastward propagating tides seen in the SABER/TIMED temperatures (2002-2007). *Advances in Space Research*, *46*, 257–274. https://doi.org/10.1016/j.asr.2010.03.026

Paulik, L. C., & Birner, T. (2012). Quantifying the deep convective temperature signal within the tropical tropopause layer (TTL). *Atmospheric Chemistry and Physics*, *12*, 12183–12195. https://doi.org/10.5194/acp-12-12183-2012

Pirscher, B., Foelsche, U., Borsche, M., Kirchengast, G., & Kuo, Y.-H. (2010). Analysis of migrating diurnal tides detected in FORMOSAT-3/COSMIC temperature data. *Journal of Geophysical Research*, *115*.D14108. https://doi.org/10.1029/2009JD013008

Podglajen, A., Plougonven, R., Hertzog, A., & Jensen, E. (2018). Impact of gravity waves on the motion and distribution of atmospheric ice particles. *Atmospheric Chemistry and Physics*, *18*, 10799–10823. https://doi.org/10.5194/acp-18-10799-2018

Randel, W. J., & Wu, F. (2005). Kelvin wave variability near the equatorial tropopause observed in GPS radio occultation measurements. *Journal of Geophysical Research*, *110*.D03102. https://doi.org/10.1029/2004JD005006

Sakazaki, T., Fujiwara, M., & Shiotani, M. (2018). Representation of solar tides in the stratosphere and lower mesosphere in state-of-the-art reanalyzes and in satellite observations. *Atmospheric Chemistry and Physics*, *18*, 1437–1456. https://doi.org/10.5194/acp-18-1437-2018

Sakazaki, T., Sato, K., Kawatani, Y., & Watanabe, S. (2015). Three-dimensional structures of tropical nonmigrating tides in a high-vertical-resolution general circulation model. *Journal of Geophysical Research - D: Atmospheres*, *120*, 1759. https://doi.org/10.1002/2014JD022464

Scherllin-Pirscher, B., Randel, W. J., & Kim, J. (2017). Tropical temperature variability and Kelvin-wave activity in the UTLS from GPS RO measurements. *Atmospheric Chemistry and Physics*, *17*, 793–806. https://doi.org/10.5194/acp-17-793-2017

Scherllin-Pirscher, B., Steiner, A. K., Anthes, R. A., Alexander, M. J., Alexander, S. P., Biondi, R., et al. (2021). Tropical temperature variability in the UTLS: New insights from GPS radio occultation observations. *Journal of Climate*. https://doi.org/10.1175/JCLI-D-20-0385.1

Schmidt, T., Alexander, P., & Torre, A. (2016). Stratospheric gravity wave momentum flux from radio occultations. *Journal of Geophysical Research - D: Atmospheres*, *121*, 4443–4467. https://doi.org/10.1002/2015JD024135

Schreiner, W. S., Weiss, J. P., Anthes, R. A., Braun, J., Chu, V., Fong, J., et al. (2020). COSMIC-2 radio occultation constellation: First results. *Geophysical Research Letters*, *47*.e2019GL086841. https://doi.org/10.1029/2019gl086841

Tsai, H.-F., Tsuda, T., Hajj, G. A., Wickert, J., & Aoyama, Y. (2004). Equatorial Kelvin waves observed with GPS occultation measurements (CHAMP and SAC-C). *Journal of the Meteorological Society of Japan*, *82*(1B), 397–406. https://doi.org/10.2151/jmsj.2004.397

Ueyama, R., Jensen, E. J., Pfister, L., & Kim, J. E. (2015). Dynamical, convective, and microphysical control on wintertime distributions of water vapor and clouds in the tropical tropopause layer. *Journal of Geophysical Research - D: Atmospheres*, *120*, 10483–10500. https://doi.org/10.1002/2015JD023318

Wang, L., & Alexander, M. J. (2010). Global estimates of gravity wave parameters from GPS radio occultation temperature data. *Journal of Geophysical Research*, *115*.D21122. https://doi.org/10.1029/2010JD013860

Wang, L., & Geller, M. A. (2003). Morphology of gravity-wave energy as observed from 4 years (1998-2001) of high vertical resolution U.S. radiosonde data. *Journal of Geophysical Research*, *108*(D16), 1. https://doi.org/10.1029/2002JD002786

Wheeler, M., & Kiladis, G. N. (1999). Convectively coupled equatorial waves: Analysis of clouds and temperature in the wavenumber-frequency domain. *Journal of the Atmospheric Sciences*, *56*, 374–399. https://doi.org/10.1175/1520-0469(1999)056<0374:ccewao>2.0.co;2

Wu, D. L., McLandress, C., Read, W. G., Waters, J. W., & Froidevaux, L. (1998). Equatorial diurnal variations observed in UARS Microwave Limb Sounder temperature during 1991-1994 and simulated by the Canadian middle atmosphere model. *Journal of Geophysical Research*, *103*, 8909–8917. https://doi.org/10.1029/98jd00530

Xie, F., Wu, D. L., Ao, C. O., & Mannucci, A. J. (2010). Atmospheric diurnal variations observed with GPS radio occultation soundings. *Atmospheric Chemistry and Physics*, *10*(14), 6889–6899. https://doi.org/10.5194/acp-10-6889-2010

Xu, X., Yu, D., & Luo, J. (2018). The spatial and temporal variability of global stratospheric gravity waves and their activity during sudden stratospheric warming revealed by COSMIC measurements. *Advances in Atmospheric Sciences*, *35*(12), 1533–1546. https://doi.org/10.1007/s00376-018-5053-1

Zeng, Z., Randel, W., Sokolovskiy, S., Deser, C., Kuo, Y.-H., Hagan, M., et al. (2008). Detection of migrating diurnal tide in the tropical upper troposphere and lower stratosphere using the Challenging Minisatellite Payload radio occultation data. *Journal of Geophysical Research*, *113*.D03102. https://doi.org/10.1029/2007JD008725

Zeng, Z., Sokolovskiy, S., Schreiner, W. S., & Hunt, D. (2019). Representation of vertical structures by radio occultation observations in the upper troposphere and lower stratosphere. Comparison to high-resolution radiosonde profiles. *Journal of Atmospheric and Oceanic Technology*. 655–670. https://doi.org/10.1175/JTECH-D-18-0105.1

Zhang, X., Forbes, J. M., & Hagan, M. E. (2010). Longitudinal variation of tides in the MLT region: 2. Relative effects of solar radiative and latent heating. *Journal of Geophysical Research*, *115*.A06317. https://doi.org/10.1029/2009JA014898

Zipser, E. J., Cecil, D. J., Liu, C., Nesbitt, S. W., & Yorty, D. P. (2006). Where are the most intense thunderstorms on Earth? *Bulletin of the American Meteorological Society*, *87*, 1057–1072. https://doi.org/10.1175/bams-87-8-1057